Structure and microrheology of genome organization: From experiments to physical modeling

Andrea Papale* and Angelo Rosa†
Sissa (Scuola Internazionale Superiore di Studi Avanzati), Via Bonomea 265, 34136 Trieste (Italy)
(Dated: June 6, 2018)

The mechanisms beyond chromosome folding within the nuclei of eukaryotic cells have fundamental implications in important processes like gene expression and regulation. Yet, they remain widely unknown. Unveiling the secrets of nuclear processes requires a cross-disciplinary approach combining experimental techniques to theoretical, mathematical and physical, modeling. In this review, we discuss our current understanding of generic aspects of genome organization during interphase in terms of the conceptual connection between the large-scale structure of chromosomes and the physics beyond the crumpled structure of entangled ring polymers in solution. Then, we employ this framework to discuss recent experimental and theoretical results on the microrheology of Brownian nanoprobes dispersed in the nuclear medium.

I. OUTLINE OF THE REVIEW

An accurate description of the mechanisms underlying the regulation of the genome in eukaryotes inevitably involves the study of the genetic code contained in the DNA string. Obviously fundamental, this information represents nonetheless only a small part of the intricate puzzle that determines the correct functioning of the entire cell. Each strand of DNA contained in a single chromosome is in fact part of the cell nucleus, and the way each chromosome is individually bent within the nucleus and in relation to the other chromosomes and the other nuclear structures is crucial to the future of the whole cell. In other words, the proper functioning of the genome of each organism is based not only on the alphabet contained in the sequence (genome in one dimension, or $1d$-genome), but also on how this sequence is folded and moves within the cell nucleus (genome "in space and time", or $4d$-genome [1, 2]).

The intricate relationship between genome structure and function within the nucleus can be now systematically explored owing to the development of high-resolution experimental techniques providing more and more accurate data for chromosome positioning and interactions [3, 4], chromosome mobilities [5, 6] and the viscoelastic properties of the nucleus and the cytoplasm [7]. At the same time, the amount of experimental data is pacing so fast to require the additional input provided by sophisticate quantitative tools as rigorous statistical methods [8], machine learning [9] and physical models [10–13] of the three-dimensional structure and dynamics of chromosomes and the nuclear and cellular environments.

In this review article, we concentrate on recent experimental progress concerning nuclear chromosome structure and dynamics and the motion of nuclear bodies and their interpretation in terms of theoretical concepts borrowed from generic polymer and soft matter physics. In particular, we highlight two fundamental aspects: the physical origin of chromosome organization explained in terms of the slow relaxation of large polymers subjected to topological constraints and the impact of nuclear structure on the Brownian diffusion of nanoprobes microinjected within the nucleus (microrheology).

The material of the review is organized as following: Sections II A and II B provide the necessary introduction to the phenomenology of chromosome organization and single-particle tracking applied to the exploration of the nucleus. In Secs. III A and III B we present general concepts and applications of polymer theory to model nuclear architecture and microrheology. Conclusions with highlights on future research topics are sketched in Sec. IV. Technical details on the general principles of microrheology and the physics of ring polymers which may be skipped at first reading are summarized in specific sections (boxes) at the end of the article.

II. NUCLEAR ORGANIZATION AND GENOME STRUCTURE

A. From DNA to chromosomes

The cells of eukaryotes are partitioned into distinct compartments (Figure 1(A)), each of which is delimited by a "wall" made of a single or double lipid layer membrane [15]. In general, each compartment has evolved to fulfil a well-defined function.

The nucleus constitutes one of these compartments (Fig. 1(B)): it consists of a roughly spherical region where the lipid bilayer enabling separation from the rest of the cell (the *nuclear envelope*) is externally connected to the cytoplasm, while the internal layer connects to the nuclear lamina. Importantly, the structure of the envelope helps the nucleus to sustain its shape. A fundamental role of the nucleus is to isolate the DNA double-helix from the rest of the cell and to protect it from physical and/or chemical damage. Inside the nucleus, the genetic

*Electronic address: andrea.papale@sissa.it
†Electronic address: angelo.rosa@sissa.it

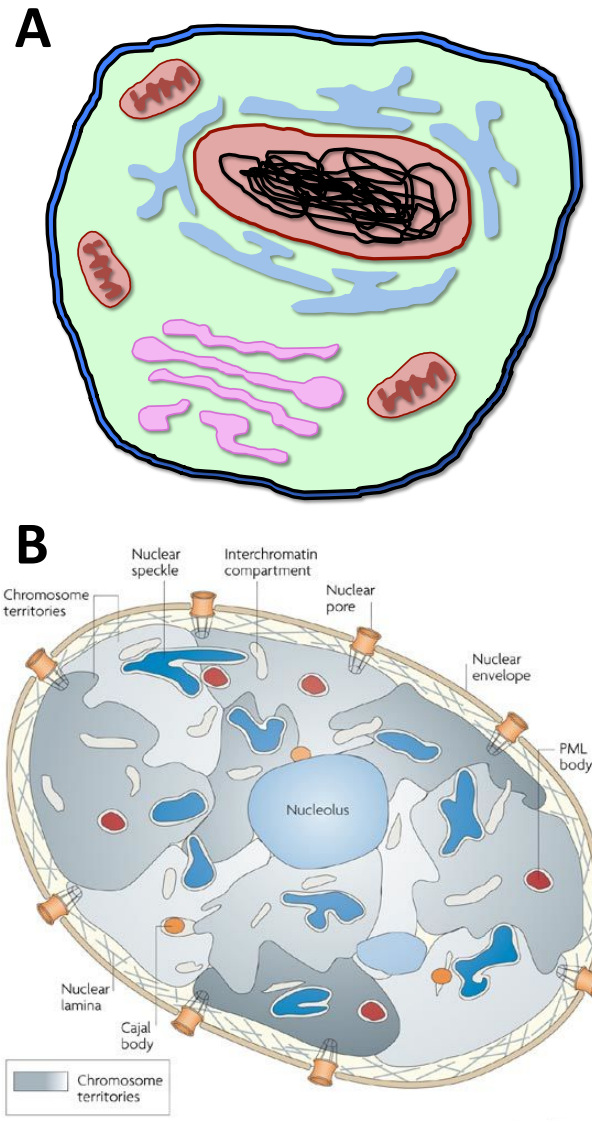

FIG. 1: (A) Schematic illustration of the typical eukaryotic cell, showing the peculiar division into physically separated compartments. The nucleus is one of this compartments, it is shown in light red at the cell's center. The black rope inside represents DNA. (B) More detailed representation of the nucleus, showing its own compartmentalization. In its inside, there exist regions void of chromatin ("interchromatin" compartments) and chromosomes condense into "territories" (see Sec. II). Reproduced with permission from Ref. [14].

information carried by DNA is decoded and then post-processed to fulfil the cellular processes.

It is now well established that, in a manner similar to proteins who must acquire a unique three-dimensional shape (the so-called "native" state) in order to accomplish their functional role [15], so the correct expression of the genetic information encoded in the linear sequence of DNA is the result of appropriate folding of the double-helix inside the nucleus [16, 17].

A vivid example of the intriguing connection between

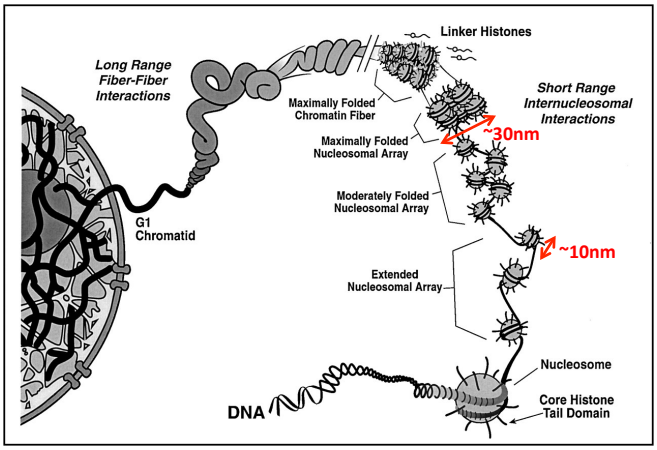

FIG. 2: Schematic illustration of DNA and chromatin fiber structure in nuclei of eukaryotic cells. The chromatin fiber originates from the wrapping of DNA around the nucleosome complex which produces the necklace-like structure known as the 10nm fiber, and the folding of 10nm fibers into 30nm fibers. The nature and very existence of the latter remains highly debated. Reproduced with permission from Ref. [24].

genome structure and function is provided by the nuclear architecture of rod photoreceptor cells in nocturnal *against* diurnal mammals [18]. The rods of diurnal retinas show the typical architecture of nearly all eukaryotic cells, with most heterochromatin (a tightly packed form of chromatin) close to the nuclear periphery and euchromatin (a gene-rich, lightly packed form of chromatin) concentrated toward the nuclear interior. Instead, the rods of nocturnal retinas display the reverse pattern of heterochromatin nearby the nuclear center and euchromatin closer to the nuclear envelope. The two opposite configurations are the results of the best adaptation of the corresponding species to the environment. At the same time, chromosome "misfolding" is typically associated to severe pathologies: for instance, fibroblasts of individuals affected by premature aging due to the Hutchinson-Gilford progeria syndrome show massive chromatin decondensation not observed in healthy cells [19–21]. Further examples include some forms of cancer [22] and other genetic dysfunctions [23].

In a typical human nucleus, about two meters (corresponding to $\approx 6\times10^9$ basepairs (bp)) of DNA are packed into distinct chromosomes, each chromosome made of a unique filament of chromatin fiber. Chromatin results from the association of the double-helix to specific protein complexes (Fig. 2). Approximately 147bp of DNA wrap around the nucleosome complex (an octamer of core histone proteins (H2A, H2B, H3, H4) [25]), forming the 10nm-wide and 6nm-thick nucleosome-core particle (ncp) [26]. Consecutive ncp's are linearly connected into the so-called "10nm" fiber by $\approx$ 50bp of "linker" DNA [24], making the typical distance between the centers of neighboring core particles of the order of "10nm + 50bp/(3bp/nm) = 25nm". The contour length density

of the 10nm fiber is hence "200bp/(25nm) = 8bp/nm", which is ≈ 3 times more compact than bare DNA. In spite of the considerable experimental work of last decades, there is little consensus concerning how chromatin folds above the 10nm fiber.

In general, *in-vitro* studies of reconstituted nucleosomal arrays have pointed out [24] the role of nucleosome-nucleosome interactions in mediating the formation of helical-like structures with diameter in the range 30 − 40nm and a contour length density of $\approx$ 100bp/nm, *i.e.* $\approx 30\times$ more compact than bare DNA. This so-called "30nm" fiber has been proposed as an essential element of the three-dimensional structures of interphase and mitotic chromosomes *in-vivo*. Yet, its true existence remains highly controversial.

In fact, recent experimental studies by Maeshima and coworkers based on small-angle X-ray scattering (SAXS) on HeLa cells [27] in combination with computational modeling essentially detected no structural features beyond the 10nm fiber. Based on these results, the authors proposed [28] then an alternative model where chromosomes in interphase nuclei look like an interdigitated polymer melt of nucleosome fibers lacking the 30nm chromatin structure (Fig. 3(A)). Very recently, these results have been substantially confirmed by chromEMT [29], a novel high-resolution experimental technique combining electron microscopy tomography (EMT) with a labeling method (ChromEM) that selectivity enhances the contrast of DNA. ChromEMT supports the picture where chromatin fibers form disordered structures packed together at different concentrations in the nucleus (Fig. 3(B)). Interestingly, although chromatin compaction is locally changing in time, measurements of density fluctuations at high-resolution reveal that nuclear chromatin behaves like a compact and dynamically "stable" *fractal* medium [30].

Although the distribution of chromatin fibers seems to display, to some extent, some degree of randomness, other notable features emerge which suggest that some order at the nuclear level does exist [33]. First, chromosome mapping by "fluorescence *in-situ* hybridization" (FISH) reveals the presence of distinct and moderately overlapping [34] regions termed "chromosome territories", see Fig. 4(A,B). Moreover, the spatial distance of each territory from the nuclear envelope is non-random, with gene poor/rich chromosomes being systematically closer to the nuclear envelope/center [35]. Second, chromatin-chromatin contacts detected by HiC [4] have shown spatial segregation of chromosome sequences the size of a few megabasepairs (Mbp) termed "A/B sub-compartments" (Fig. 4(C)). The data suggest that sub-compartments tend to interact more if they are alike than if they are not, and that A/B compartments correlate with (tissue-dependent) active/inactive chromatin. Third, chromosomes result partitioned into *topologically-associating domains* (TADs, Fig. 4(C)) of linear size $\lesssim 1$ Mbp: within a TAD, DNA sequences interact more frequently with each other than with sequences outside the TAD [32]. Remarkably, TADs appear well conserved across tissues *within* the same species [36] and even *between* different species [37].

To conclude, the phenomenology described can be so summarized: nuclear chromatin fibers form an intricate polymer-like network at small chromatin scales, with "vague" echoes of ordered structures starting from intermediate to large spatial scales (TADs $\rightarrow$ A/B-compartments $\rightarrow$ territories).

The next question is then how such intricacy affects and is affected by another important ingredient of nuclear organization: the presence of macromolecular complexes and enzymes which move through the nucleus directed towards specific DNA target binding sequences [38, 39]. In the next section, we discuss the connection between chromatin folding and the diffusion of nuclear complexes from the point of view of *microrheology*, one of the most versatile and powerful experimental tool available nowadays.

B. Microrheology of the nucleus

Microrheology is based on the tracking of the Brownian motion of fluorescent nanoprobes injected inside the cytoplasm or the nucleus. From nanoprobe motion, one extracts the time (τ) mean-square displacement (MSD) of the probe, $\langle \Delta x^2(\tau) \rangle$, which is used then as a proxy for the viscoelastic properties of the embedding medium (see Box 1 and Refs. [7, 40–43] for details).

In fact, the MSD constitutes an important source of information concerning the nature of the environment [44]. For instance, in a thermally fluctuating, purely viscous medium, nanoprobe motion is described by standard diffusion with $\langle x^2(\tau) \rangle \sim D\tau$ where D is the diffusion coefficient. Instead, in complex and disordered media [44–46], nanoprobes can behave quite differently: in general, $\langle x^2(\tau) \rangle \sim D_\alpha \tau^\alpha$ with $\alpha \neq 1$ and D_α is the "generalized" diffusion coefficient.

Particularly relevant to the cellular context is the case of *subdiffusion* with $0 < \alpha < 1$. In fact, a growing number of experimental studies employing single-particle tracking of fluorescently-labeled chromatin loci [5, 6] has demonstrated that loci dynamics is typically subdiffusive [47] and, at least in some cases, ATP-dependent [48, 49]. From the physical point of view, subdiffusion can be ascribed either to the macromolecular crowding of the nucleus [50, 51] which obstructs free chromatin motion or to the polymer-like nature of the chromatin fiber [52], or, most likely, to a combination of both.

Subdiffusion is also an important feature emerging in microrheological studies of tracked nanoprobes within the cytoplasm or the nucleus. However, the literature on this topic is surprisingly much more limited than the one on single-particle tracking of chromosome loci.

To our knowledge, the first microrheological studies in live cells are ascribable to Tseng *et al.* [40, 53] who measured the viscoelastic properties of the cytoplasm and the

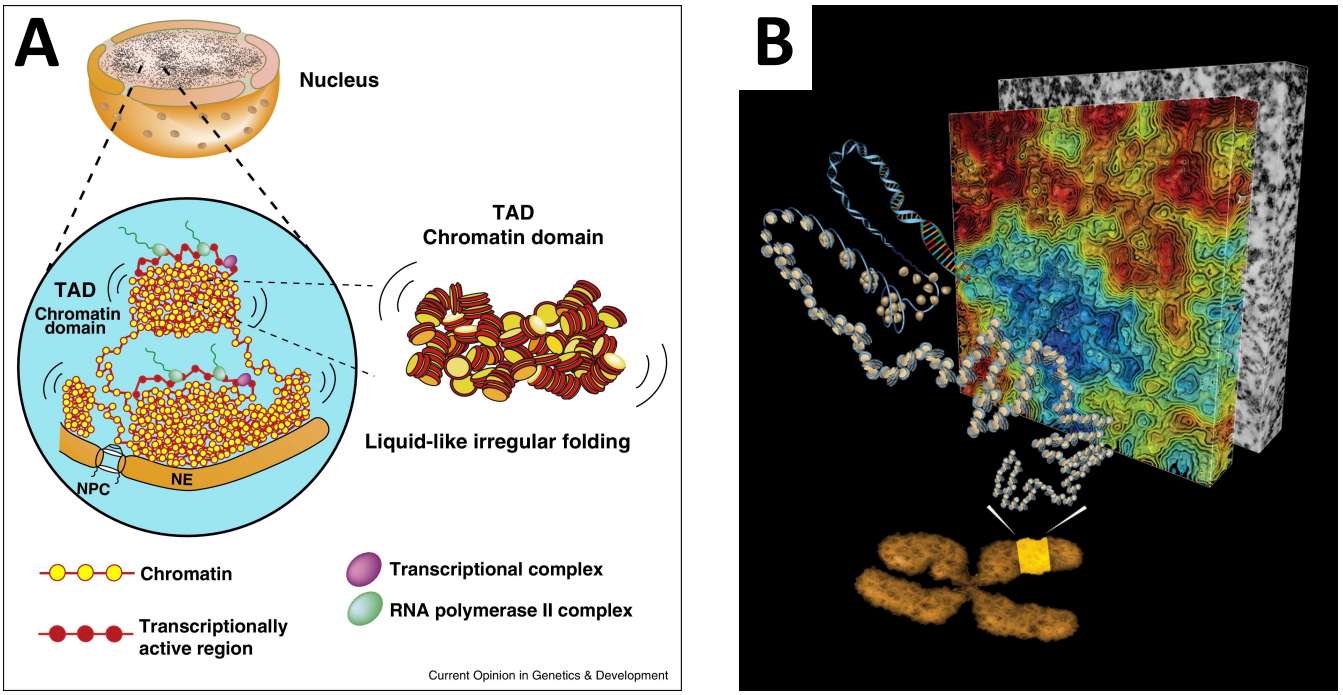

FIG. 3: (A) Polymer melt-like model by Maeshima and coworkers [27, 28] of the eukaryotic nucleus filled by interdigitated 10nm chromatin fibers. Topologically-associating domains (TADs) partition the genome into regions where chromatin-chromatin contacts (see also Fig. 4(C)) are more intense between the elements of the same region than between elements belonging to different regions. Reproduced with permission from [28]. (B) ChromEMT [29] reveals that chromatin forms a disordered $3d$ structure with regions of variable concentrations from high (red) to low (blue). Reproduced with permission from [29].

intranuclear region of mouse cells (Swiss 3T3 fibroblasts). Yellow-green fluorescent spherical nanoprobes of diameter = 100nm were microinjected within the cytoplasm and their trajectories tracked inside the nucleus and the perinuclear region of the cytoplasm.

There are important differences in the two situations. Nanospheres fluctuating in the crowded nuclear region have trajectories which do not overlap, showing "caged-and-escape" motion. On the contrary, nanospheres moving inside the cytoplasm show extensive overlap. The corresponding MSDs reflect these differences: MSD of nanoprobes diffusing inside the nucleus grows with τ on short time scales ($[0-0.1]$ seconds), then shows a plateau ($[0.1-1]$ s), and finally grows again at large lag-times, in agreement with the "caged-and-escape" motion between confining domains of average linear size $\approx$ 290nm. Conversely, the plateau displayed by cytoplasmic nanospheres takes a higher value and reflects the restricted motion inside the cell. Finally, MSDs were used (Box 1) to calculate the complex shear modulus whose real ($G'(\omega)$, full symbols) and imaginary ($G''(\omega)$, open symbols) parts correspond to the storage and loss moduli of the medium embedding the nanoprobes. Qualitatively, the curves for the cytoplasm and the nucleoplasm have similar shapes. Quantitatively, by comparing the plateau values for $G'(\omega)$ the nucleoplasm is $\approx 2\times$ stiffer under shear than the cytoplasm. Moreover, the low viscosity of the cytoplasm compared to the nucleus should facilitate the transport of proteins and molecules from and to the nucleus. At the same time, nuclear viscosity, higher if compared to cytoplasm, might play an active role in chromosome reorganization during interphase.

While the work by Tseng *et al.* focuses on passive diffusion within the cytoplasm or the nucleus, the motion of a large number of macromolecular nuclear bodies and subnuclear organelles like transcription compartments (TCs), promyelocytic leukemia (PML) nuclear bodies or Cajal bodies (CBs) which are involved in transcriptional regulation or RNA processing results from the combination of both, passive and active (*i.e.*, energy-consuming) processes [55–57]. Moreover, recent work in bacteria [48] suggests that consumption of ATP increases the mobility of cellular bodies and chromatin more steeply with temperature in untreated cells than in ATP-depleted cells.

In order to understand the role of active processes on nuclear dynamics and the motion of nuclear bodies, Hameed *et al.* [54] compared the passive motion of nanoprobes to the driven motion of transcription compartments (TCs). TCs are chromatin domains with an open chromatin structure which partially colocalize to active "transcription factories". During this process and at physiological temperatures (37°C), they undergo directed movements which are influenced by ATP-dependent chromatin remodeling processes [58], and which are suppressed at lower, non-physiological temperatures.

To characterize the motion of TCs, Hameed *et al.*

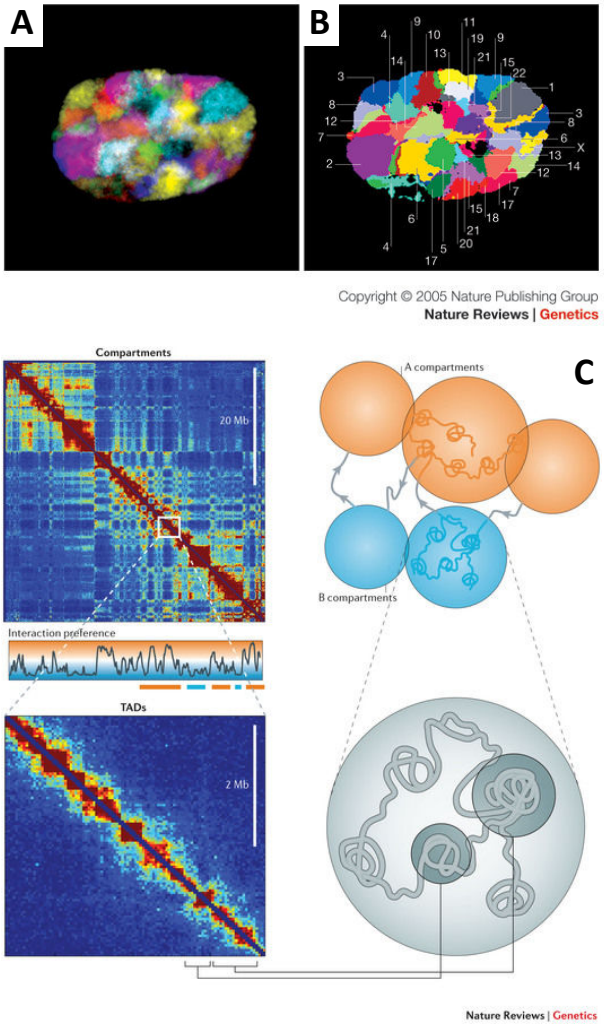

FIG. 4: Chromosome organization is hierarchical from territories down to macro-domains and TADs. (A,B) Territorial organization of the human nucleus is visualized by FISH by using a combination labelling scheme in which each chromosome is labelled with a different set of fluorochromes. In this way, each chromosome territory can be identified by the corresponding combination of different colors and, then, appropriately annotated by its corresponding number. Reproduced with permission from [31]. (C) HiC shows an extensive network of chromatin-chromatin contacts within the genome. These interactions can be represented in the form of matrices showing a characteristic patterning into tissue-specific macro-domains ($\gtrsim$ 1 megabasepairs (Mbp)) of active/inactive (A/B) chromatin [4], and tissue-independent micro-domains ($\lesssim$ 1 Mbp) termed TADs [32]. DNA interact more frequently intra-TAD than inter-TAD. Reproduced with permission from [10].

tracked tens of nanoprobes of linear size = 1μm microinjected within the nuclei of HeLa cells at 25°C by using a protocol similar to the one by Tseng *et al.* (Fig. 5(A)). The results are in quantitative agreement with those reported in the former work, in particular nanoprobe motion is caged within domains of linear size $\approx$ 250nm (Fig. 5(B)), a value remarkably close to the one ($\approx$ 290nm) measured by Tseng *et al.* in murine fibroblasts. Furthermore, single trajectories can be clustered into two groups according to the long-time behaviors of corresponding MSDs: in the first group, MSDs are plateauing at large times while in the second they steadily increase (Fig. 5(C-E)). The analysis is finally completed by computing the storage and loss moduli, $G'(\omega)$ and $G''(\omega)$ (Fig. 5(F)): the nucleus behaves like a "power-law" solid ($G' > G''$) at low frequencies (again, in qualitative agreement with the experiments by Tseng *et al.*) crossing to viscous-like behavior at large frequencies. The procedure was then repeated at 37°C with analogous results.

Next, passive nanoprobe motion was compared to the motion of TCs at the same two temperatures. As anticipated above, at the non-physiological temperature of 25°C, TC motion loses directionality and becomes similar to passive motion of nanoprobes with analogous confinement and dispersion of MSD curves (Fig. 5(G,H)). Conversely, trajectories taken at 37°C display "mixed" behavior of confined motion and jumps between close-by cages (Fig. 5(I,J), analogous to the results for passive nanoprobes in murine fibroblasts discussed before and significantly larger mobility (Fig. 5(K)). Accordingly (Fig. 5(L)), curves for storage and loss moduli at 25°C are qualitatively similar to the ones for passive nanoprobes, while at the higher temperature they show a drastic change with the nuclear environment becoming sensibly much softer to TC motion. The temperature dependent behavior is dramatically affected by ATP-depletion and perturbations to chromatin remodeling processes [54], suggesting that TC motion is partially stimulated by an active component.

Interestingly, the dynamic behavior of TCs constrasts analogous results [56] for the motion of Cajal bodies (CBs) in healthy (normal) and ATP-depleted nuclei. CBs are dynamic structures implicated in RNA-related metabolic processes. They can diffuse inside the nucleus, merge or split to form larger or smaller CBs and even associate/dissociate with/from specific genomic loci [56]. These processes were investigated in normal cells and in ATP-depleted cells in order to quantify the role of ATP in CB dynamics (see Fig. 6). Typically, CBs show anomalous diffusion while moving within interchromatin nuclear compartment. Quite unexpectedly, upon ATP depletion CBs tend to diffuse faster and they are no longer associated with dense chromatin regions. In conclusion, the association between CB and chromatin is an active process needing ATP.

To summarize, these results illustrate the prominent role of microrheology in the characterization of nuclear organization and how this influences the motion of nuclear bodies which participate to the correct functioning of cellular processes. In the next section, we discuss the connection between the physics of solutions of crumpled polymers and chromosome structure and dynamics, and illustrate its implications in the theoretical description of nuclear microrheology.

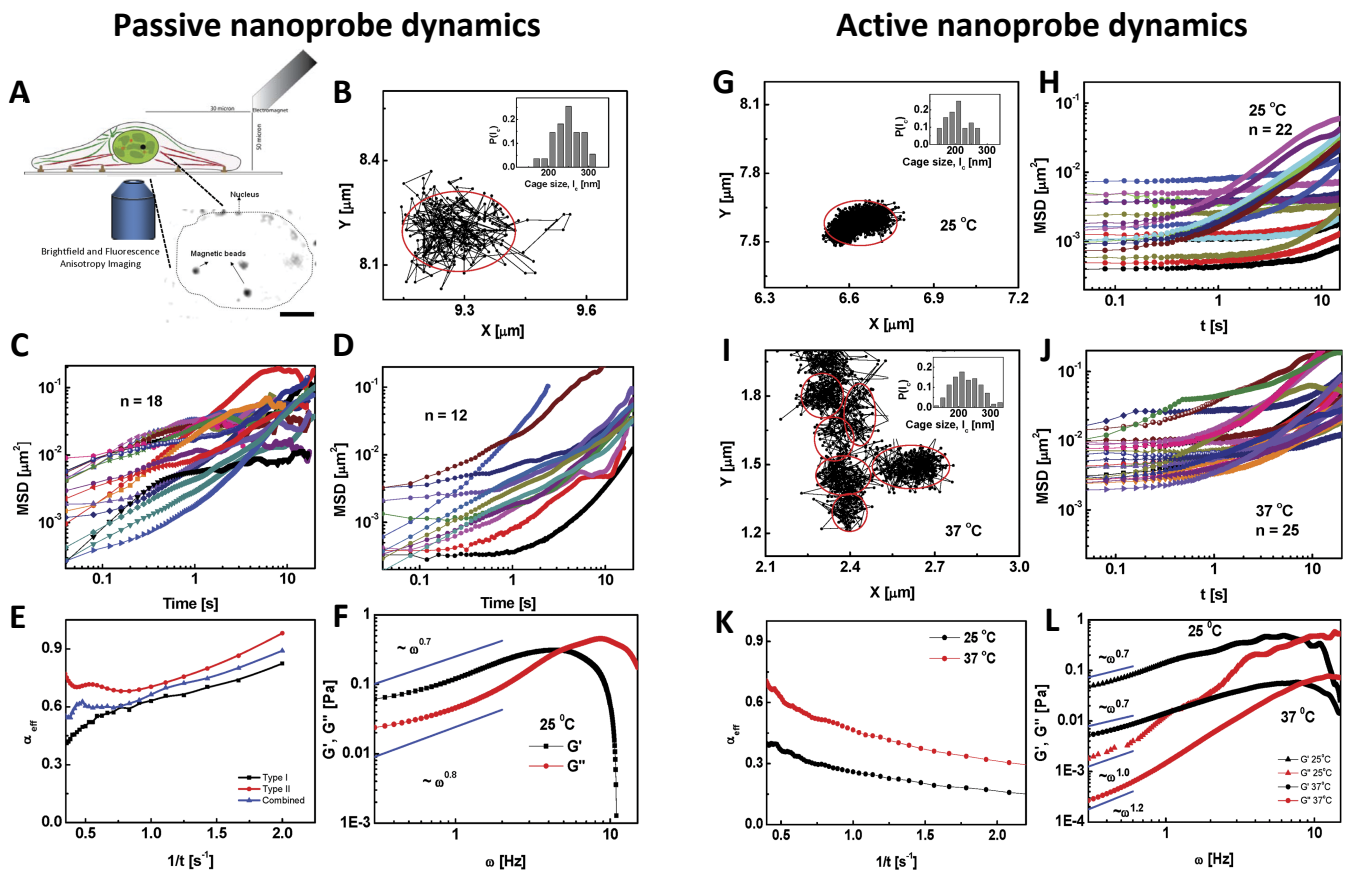

FIG. 5: Microrheology of mammalian nuclei (live HeLa cells (human)): passive (A-F) *vs.* active (G-L) dynamics. (A) Schematic illustration of the experimental setup used for single-particle tracking. Inset: focus on microinjected probes tracked by fluorescence microscopy. (B) Typical trajectory of a nanoprobe at 25°C showing diffusion in a confined cage. Inset: Histogram of cage sizes l_c. (C,D) Time mean-square displacements (MSDs) for different nanoprobes, displaying behavior I (C, plateauing at large times) and II (D, monotonically increasing). (E) Mean effective exponents α_{eff} (MSD(τ) $\sim \tau^{\alpha_{eff}}$) as a function of inverse time for trajectories I and II and their combination. (F) Storage and loss moduli, $G'(\omega)$ and $G''(\omega)$ as functions of frequency ω. At low ω's the nucleus is elastic ($G' > G''$) while becoming increasingly viscous at higher ω's. (G) Typical trajectory of a transcription compartment (TC) at 25°C showing diffusion in a confined cage as for microinjected beads. Inset: Histogram of cage sizes l_c. (H) Time MSDs for different TCs at 25°C. (I) Typical trajectory of a TC at 37°C showing diffusion in confined cages intermitted with jumps even across long distances. (J) Time MSDs for different TCs at 37°C. (K) Mean effective exponents α_{eff} as functions of inverse time for the two temperatures. (L) Storage and loss moduli, $G'(\omega)$ and $G''(\omega)$, as functions of frequency ω for the two temperatures. Reproduced from [54] under Creative Commons License.

III. POLYMER MODEL OF NUCLEAR CHROMOSOME ORGANIZATION

A. "Topological" origin of chromosome territories

In spite of their intrinsic complexity (discussed in Secs. II and II B), the general behavior of interphase chromosomes is remarkably well described by generic polymer physics [11–13, 66–71].

To fix the ideas, we start from a set of experiments dated back to the 60-70's featuring very accurate estimates of nuclear volumes (NV, in micrometers^3 (μm^3)) from different organisms compared to the sizes of the corresponding genomes (GS, in basepairs (bp)). The data are summarized in Table I (animals) and Table II (plants). Remarkably, the data fit well (see Fig. 7) to the *linear* relationship "GS $\sim$ NV". Moreover, this law appears to be the same for animals and plants including the prefactor which, within statistical fluctuations (see Fig. 7, inset), suggests a rather robust DNA density of $\rho \approx (0.054 \pm 0.028)$bp/nm^3. This value corresponds to a volume occupancy from $\approx 7\%$ (for DNA being modeled as a cylinder of 2.2nm of diameter with linear density of $\approx$ 3bp/nm [15]) up to $\approx 25\%$ (for chromatin being modeled as a cylinder of 30nm of diameter with linear density of $\approx$ 100bp/nm, see Sec. II).

Under these conditions and supported by experimental observations on the polymer-like nature of the chromatin fiber (Sec. II), the theory of semi-dilute polymer solutions [74] represents a good starting point for a quanti-

Animals

Organism	Nuclear volume [μm^3]	Nuclear radius [μm]	Genome size [$\times 10^9$ bp]	Genome density [bp/nm^3]
Anurans, liver parenchymal cells [59]				
A. obstetricans	253	3.92	20.54	0.081
X. laevis	125	3.10	7.34	0.059
B. marinus	221	3.75	9.49	0.043
B. viridis	122	3.08	10.47	0.086
B. fowleri	157	3.35	12.32	0.079
B. bufo	231	3.81	13.89	0.060
B. calamita	123	3.09	9.00	0.073
B. americanus	136	3.19	10.56	0.078
H. squirella	137	3.20	10.17	0.074
H. septentrionales	107	2.95	4.30	0.040
R. pipiens	168	3.42	14.67	0.087
R. catesbiana	225	3.77	14.87	0.066
R. temporaria	129	3.14	8.61	0.067
R. esculenta	196	3.60	13.79	0.070
Salamanders, liver parenchymal cells [59, 60]				
N. maculosus	1784	7.52	192.47	0.108
P. anguinus	1223	6.63	102.79	0.084
A. tigrinum	1104	6.41	83.42	0.076
A. mexicanum	943	6.08	75.31	0.080
A. means	3852	9.73	188.56	0.049
N. viridescens	943	6.08	91.15	0.097
T. granulosa	716	5.55	66.50 ± 5.87	0.093 ± 0.008
T. cristatus	697	5.50	51.35	0.074
T. vulgaris	768	5.68	69.44	0.090
T. alpestris	730	5.59	73.55	0.101
D. fuscus	523	5.00	35.21	0.067
E. bislineata	1236	6.66	72.37	0.059
P. ruber	579	5.17	48.90 ± 1.96	0.085 ± 0.003
Other organisms [61]				
N. viridescens (lens)	4174	9.99	93.50	0.022
T. cristatus (heart)	1748	7.47	58.29	0.033
R. pipiens (embryo)	627	5.31	14.02	0.022
X. laevis (kidney)	294	4.13	7.51	0.026
X. laevis (heart)	307	4.19	7.51	0.025
S. holbrooki (heart)	197	3.61	3.70	0.019
P. crinitus (lung)	153	3.32	6.16	0.040
M. musculus	435	4.70	13.50	0.031
H. sapiens (lymphocytes)	232	3.81	6.10	0.026
H. sapiens (lung)	170	3.44	6.10	0.036
H. sapiens (HeLa, cervix)	374	4.47	10.45	0.028
C. sabaeus (kidney)	421	4.65	13.65	0.032
C. griseus (ovary)	188	3.55	5.87	0.031
G. gallus domesticus (embryo)	210	3.69	2.62	0.013
T. pyriformis	678	5.45	15.36	0.023
D. melanogaster (imaginal disc)	78	2.65	0.29	0.004
S. cerevisiae	3.3	0.92	0.02	0.005

TABLE I: List of nuclear volumes (NV, in micrometers^3 (μm^3)), nuclear radii ($\equiv \left(\frac{3}{4\pi}\mathrm{NV}\right)^{1/3}$, in μm), genome sizes (GS, in base-pairs (bp)) and genome densities ($\equiv \frac{GS}{NV}$) for different animal species or different cell types of the same species. Corresponding sources are indicated at the top of each sub-panel.

Plants

Organism	Nuclear volume [μm^3]	Nuclear radius [μm]	Genome size [$\times 10^9$ bp]	Genome density [bp/nm^3]
		Higher plants [62]		
K. daigremontiana	105.0 ± 3.8	2.93 ± 0.04	10.76 ± 0.98	0.103 ± 0.013
R. sativus	111.0 ± 2.9	2.98 ± 0.03	4.89 ± 0.98	0.044 ± 0.010
R. sanguineus	120.0 ± 3.9	3.06 ± 0.03	4.89 ± 0.98	0.041 ± 0.010
T. majus	152.0 ± 4.4	3.31 ± 0.03	10.76 ± 0.98	0.071 ± 0.009
V. angustifolia	186.0 ± 5.8	3.54 ± 0.04	9.78 ± 0.98	0.053 ± 0.007
R. stenophyllus	212.0 ± 6.2	3.70 ± 0.04	11.74 ± 0.98	0.055 ± 0.006
R. obtusifolius	217.0 ± 6.9	3.73 ± 0.04	7.82 ± 0.98	0.036 ± 0.006
R. longifolius	249.0 ± 9.3	3.90 ± 0.05	12.71 ± 1.96	0.051 ± 0.010
C. nipponicum	270.0 ± 10.2	4.01 ± 0.05	43.03 ± 4.89	0.159 ± 0.024
G. sp. HV mansoer	281.0 ± 8.5	4.06 ± 0.04	5.87 ± 0.98	0.021 ± 0.004
H. annuus	293.0 ± 10.7	4.12 ± 0.05	15.65 ± 1.96	0.053 ± 0.009
C. jackmannii	347.0 ± 15.0	4.36 ± 0.06	21.52 ± 0.98	0.062 ± 0.006
Chrysanthemum sp. I	360.0 ± 10.9	4.41 ± 0.05	36.19 ± 6.85	0.101 ± 0.022
N. demascena	392.0 ± 12.8	4.54 ± 0.05	27.38 ± 1.96	0.070 ± 0.007
C. yezoense	478.0 ± 16.4	4.85 ± 0.06	28.36 ± 1.96	0.059 ± 0.006
T. blossfeldiana	481.0 ± 16.8	4.86 ± 0.06	39.12 ± 2.93	0.081 ± 0.009
V. faba	521.0 ± 14.1	4.99 ± 0.05	43.03 ± 7.82	0.083 ± 0.017
N. tazetta	579.0 ± 20.6	5.17 ± 0.06	30.32 ± 1.96	0.052 ± 0.005
A. cepa HV excel	621.0 ± 24.6	5.29 ± 0.07	52.81 ± 5.87	0.085 ± 0.013
T. sp. golden harvest	844.0 ± 23.4	5.86 ± 0.05	70.42 ± 7.82	0.083 ± 0.012
S. sibirica HV alba	908.0 ± 42.8	6.01 ± 0.09	71.39 ± 20.54	0.079 ± 0.026
Tradescantia sp. I	916.0 ± 27.6	6.02 ± 0.06	57.70 ± 4.89	0.063 ± 0.007
T. paludosa	947.0 ± 36.6	6.09 ± 0.08	52.81 ± 5.87	0.056 ± 0.008
L. squamigera	1017.0 ± 24.0	6.24 ± 0.05	125.18 ± 11.74	0.123 ± 0.015
Chrysanthemum sp. II	1183.0 ± 44.9	6.56 ± 0.08	77.26 ± 9.78	0.065 ± 0.011
T. virginiana	1324.0 ± 38.8	6.81 ± 0.07	113.45 ± 7.82	0.086 ± 0.008
L. longiflorum I	1347.0 ± 44.8	6.85 ± 0.08	103.67 ± 13.69	0.077 ± 0.013
C. lacustre	1663.0 ± 53.8	7.35 ± 0.08	138.88 ± 7.82	0.084 ± 0.007
T. paludosa	1767.0 ± 96.7	7.50 ± 0.14	115.40 ± 16.63	0.065 ± 0.013
L. longiflorum II	2809.0 ± 158.1	8.75 ± 0.16	173.11 ± 19.56	0.062 ± 0.011
		Herbaceous angiosperms [63, 64]		
A. thaliana	32 ± 3	1.97 ± 0.06	0.59 ± 0.27	0.018 ± 0.010
L. maritima	49 ± 5	2.27 ± 0.08	1.08 ± 0.04	0.022 ± 0.003
C. arietinum	96 ± 5	2.84 ± 0.05	1.86	0.019 ± 0.001
N. lutea	139 ± 7	3.21 ± 0.05	1.89	0.014 ± 0.001
S. oleracea	156 ± 7	3.34 ± 0.05	2.01	0.013 ± 0.001
A. pulsatilla	435 ± 27	4.70 ± 0.10	34.03	0.078 ± 0.005
T. navicularis	552 ± 27	5.09 ± 0.08	53.97 ± 3.65	0.098 ± 0.011
C. majalis	710 ± 17	5.53 ± 0.04	33.22	0.047 ± 0.001
F. lanceolata	1466 ± 115	7.05 ± 0.19	89.24	0.061 ± 0.005
F. camschatcensis	1824 ± 103	7.58 ± 0.14	109.78	0.060 ± 0.003
L. longiflorum	3273 ± 167	9.21 ± 0.16	68.85	0.021 ± 0.001
S. formosissima	4638 ± 262	10.35 ± 0.20	128.01	0.028 ± 0.002
		Gymnosperms [64, 65]		
P. strobus I	1468 ± 94	7.05 ± 0.15	50.17	0.034 ± 0.002
P. strobus II	1259 ± 51	6.70 ± 0.09	50.17	0.040 ± 0.002
P. glauca I	1137 ± 52	6.48 ± 0.10	31.59	0.028 ± 0.001
A. balsamea	1114 ± 62	6.43 ± 0.12	32.08	0.029 ± 0.002
L. laricina	1110 ± 55	6.42 ± 0.11	18.58	0.017 ± 0.001
P. ponderosa	1095 ± 51	6.39 ± 0.10	47.34	0.043 ± 0.002
P. resinosa	1084 ± 59	6.37 ± 0.12	46.55	0.043 ± 0.002
Ts. canadensis I	1077 ± 67	6.36 ± 0.13	36.38	0.034 ± 0.002
P. abies	1023 ± 61	6.25 ± 0.12	39.14	0.038 ± 0.002
P. glauca II	1014 ± 47	6.23 ± 0.10	31.59	0.031 ± 0.002
P. pungens	977 ± 38	6.16 ± 0.08	35.50	0.036 ± 0.001
P. glauca III	953 ± 37	6.11 ± 0.08	31.59	0.033 ± 0.001
Ts. canadensis II	852 ± 41	5.88 ± 0.09	36.38	0.043 ± 0.002
L. leptolepis	844 ± 42	5.86 ± 0.10	25.82	0.031 ± 0.002
T. media I	645 ± 28	5.36 ± 0.08	22.01 ± 0.39	0.034 ± 0.002
P. douglasii	742 ± 29	5.62 ± 0.07	37.26	0.050 ± 0.002
Ta. canadensis	677 ± 28	5.45 ± 0.08	22.69	0.034 ± 0.001
T. media II	493 ± 23	4.90 ± 0.08	22.01 ± 0.39	0.045 ± 0.003
S. giganteum	431 ± 21	4.69 ± 0.08	19.41	0.045 ± 0.002
T. occidentalis	358 ± 19	4.41 ± 0.08	24.17	0.068 ± 0.004

TABLE II: Notation is as in Table I.

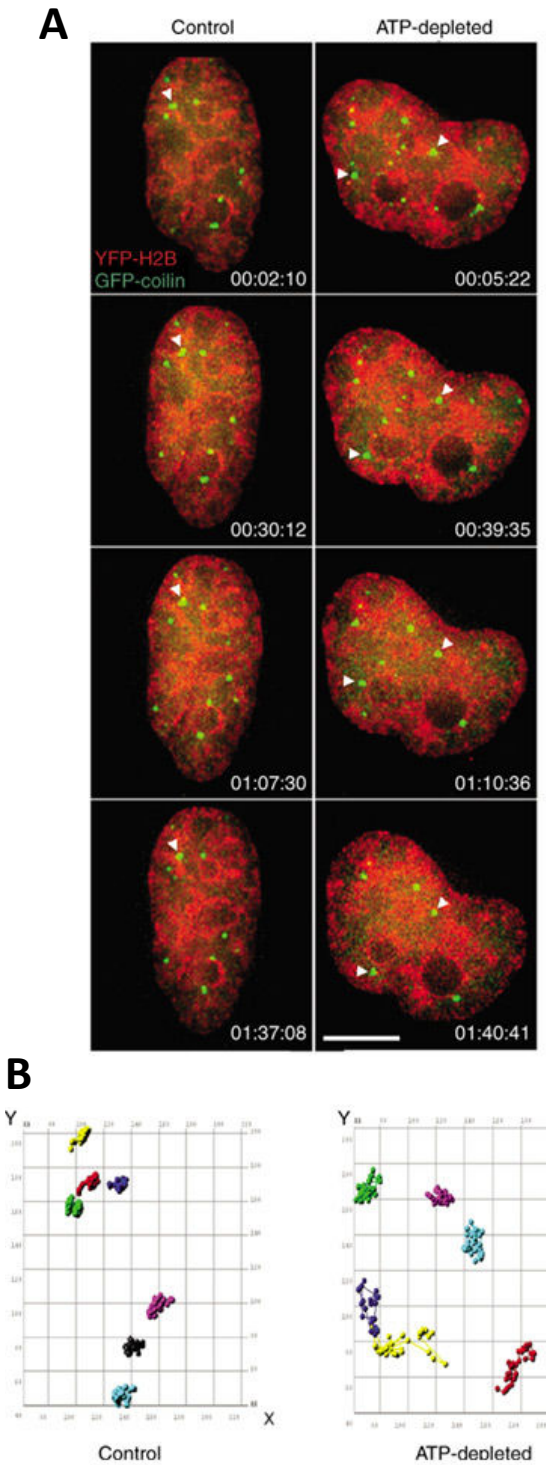

FIG. 6: Diffusion of Cajal bodies (CBs) through the nuclear interchromatin space is an APT-dependent process. (A) Examples of consecutive temporal frames of nuclei of HeLa live cells: a healthy (control) nucleus (left) *vs.* an ATP-depleted nucleus (right). CBs are stained green, while chromosomal DNA is stained red. Consecutive positions of CBs are indicated by the white arrowheads. CBs in ATP-depleted nuclei show higher mobility and they are no longer associated with dense chromatin regions. Scale bar = 10μm. (B) Reconstructed trajectories of individual CBs. Different colors correspond to different CBs. Reproduced with permission from [56].

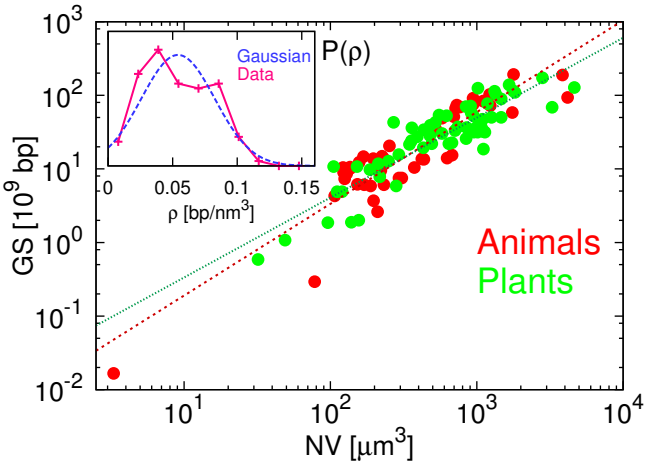

FIG. 7: Scatter plot of the genome-size (GS) *vs.* nuclear volume (NV). Detailed data for animals and plants families are summarized in Tables I and II, respectively. Lines correspond to best fits of the two sets of data to $GS = \alpha NV^{\gamma}$, which give $\gamma_{animals} = 1.25 \pm 0.09$ and $\gamma_{plants} = 1.08 \pm 0.07$. Inset: Probability distribution function for genome density $P(\rho)$ (solid curve) is well described by the Gaussian function with same average and standard deviation (dashed curve).

tative description of chromosome organization inside the nucleus.

At the beginning of interphase, each chromosome evolves from its initial, compact mitotic conformation and starts swelling inside the nucleus (Fig. 8(A)). Rosa and Everaers [72] argued that the time to reach the *complete* mixing of all chromosomes starting from the fully *unmixed* state can be estimated by assuming ordinary reptation dynamics [74, 75] for linear polymers in concentrated solutions: $\tau_{mix} \approx \tau_e \left(\frac{L_c}{L_e}\right)^3$ where $\tau_e \approx 32$ seconds and $L_e \approx 0.12$ megabasepairs (Mbp) are, respectively, the entanglement time and entanglement length of the chromatin fibers solution (Table III). With typical mammalian chromosomes of total contour length L_c of the order of 10^2 Mbp (Table I), τ_{mix} is exceeding by orders of magnitude the typical cell life time. As a consequence, the spatial structures of chromosomes remain effectively stuck into territorial-like conformations retaining the topological "memory" of the initial mitotic state.

These considerations were adapted into a generic bead-spring polymer model [72] taking into account the density, stiffness and local topology conservation of the chromatin fiber (Table III). Extensive Molecular Dynamics computer simulations then showed that the swelling of model mitotic-like chromosomes (Fig. 8(B)) leads to compact territories with physical properties akin to crumpled conformations of ring polymers in entangled solutions (Box 2). The analogy between chromosome territories and ring polymers motivated the formulation of the efficient multi-scale algorithm described in [73] which is capable of generating hundreds of putative chromo-

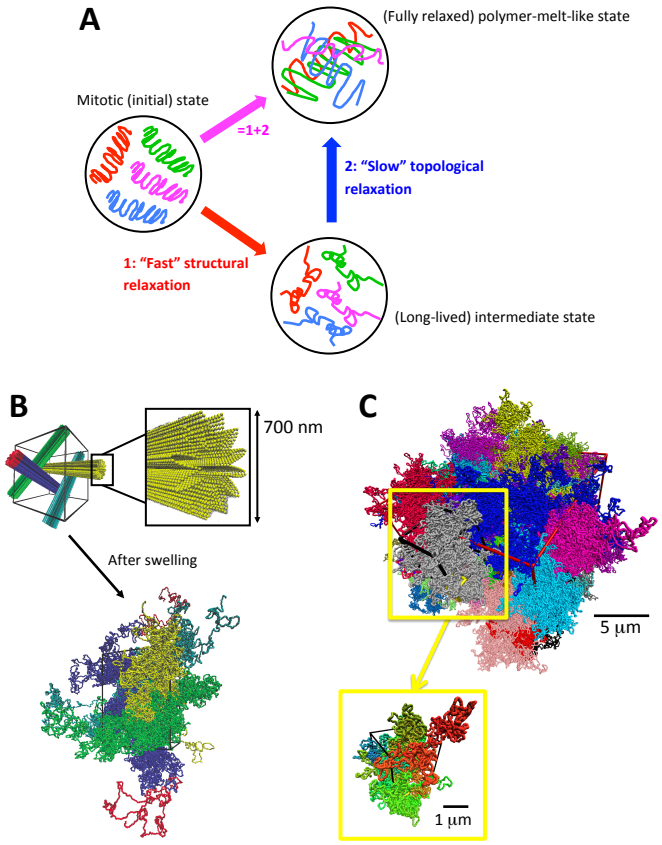

FIG. 8: "Topological" model for chromosome territories. (A) At the beginning of interphase, condensed mitotic chromosomes start swelling. The path to full relaxation and complete mixing cannot take place on natural time scales due to "slow" relaxation of the topological degrees of freedom [72]. Chromosome structures thus remain effectively quenched into separated territories which retain "memory" of the initial conformations. (B) Numerical implementation of the model by Molecular Dynamics (MD) computer simulations [72]. Model chromosomes are initially prepared into non-overlapping mitotic-like structures. MD simulations show the rapid relaxation of polymer length scales up to the tube diameter d_T, while larger length scales fold into a crumpled structure resembling the behavior of ring polymers (Box 2). Each color corresponds to a single model chromosome. Reproduced from [72] under Creative Commons License. (C) The analogy between solutions of ring polymers and chromosome territories can be systematically exploited owing to an efficient coarse-grain protocol [73] which allows to obtain hundreds of independent model conformations of mammalian-sized chromosomes. The model can be mapped to *real* time and length scales (see bars) with no free parameter [72, 73]. The snapshot here provides a typical view for a model human nucleus. Reproduced with permission from [73].

some conformations (see Fig. 8(C) for a single example) in negligible computer time. The polymer model was shown to reproduce the experimentally observed behavior of (sequence-averaged [71]) properties of interphase chromosomes: these include chromosomes spatial positions measured by FISH, chromatin-chromatin interaction data and time mean-square displacements of chromosome loci [71, 72, 78, 79].

Physical parameters of the "bead-spring" polymer model by Rosa and Everaers [72, 73].

$\rho_{\rm DNA}$	$0.012{\rm bp/nm}^3$
$\rho_{\rm 30nm}$	$1.2\cdot10^{-4}/{\rm nm}^2$
ℓ_K (30nm fiber)	$300{\rm nm}=30{\rm kbp}$
ξ	90nm
$\frac{L_e}{\ell_K}=\left(\frac{20}{\rho_{\rm 30nm}\,\ell_K^2}\right)^2$	$4\ell_K=1200{\rm nm}=0.12{\rm Mbp}$
$d_T=\sqrt{\frac{\ell_K L_e}{6}}$	245nm
τ_e	32s

TABLE III: $\rho_{\rm DNA}$, DNA density calculated for an "average" human nucleus of 5μm radius; $\rho_{\rm 30nm}$, 30nm chromatin fiber density assuming fiber compaction of 100bp/nm (Sec. II A); ℓ_K, Kuhn length of the 30nm fiber [76]; ξ, average distance from a monomer on one chain to the nearest monomer on another chain ("correlation length" [74]); L_e, entanglement length obtained from the condition of "optimal packing" of 20 chains per entanglement volume by Kavassalis and Noolandi [77]; d_T, average spatial distance between entanglements ("tube diameter" [74]); τ_e, time scale marking the onset of entanglement effects.

For illustration purposes, the single chromosome structure is described through the structure factor [74] $S(q)\equiv\langle e^{i\vec{q}\cdot(\vec{r}_i-\vec{r}_j)}\rangle$ as a function of the norm of the wave vector $q\equiv|\vec{q}|$ (Fig. 9(A)). $\vec{r}_i$ are the spatial positions of chromosome loci and average is taken over all chromosome conformations. For wave vectors $q\lesssim\frac{2\pi}{d_T}$ where $d_T\approx 245$nm is the tube diameter of the chromatin fiber [72, 78] $S(q)\sim q^{-3}$, which corresponds to the expected result for a compact, scale-free polymer.

While $S(q)$ provides information on single-chain properties, it is instructive to look at the spatial relationship between different territories. To this purpose, we consider the average DNA density at spatial distance r from the chromosome centre of mass and its two components (Fig. 9(B)): the self-density contribution from the given chromosome ($\rho^{\rm self}_{\rm DNA}(r)$) and the external contribution from the surrounding chromosomes ($\rho^{\rm ext}_{\rm DNA}(r)$). The plots demonstrate that chromosomes are rather "soft": as for common polymer systems [80], the core of each chromosome contains a significant amount of DNA protruding from close-by chains. In summary territoriality is not a preclusion for chromosome strands to intermingle with each other, in agreement with cryo-FISH experiments [34].

B. Microrheology of the nucleus

It is indeed quite remarkable that, separately, Tseng *et al.* [40] and Hameed *et al.* [54] reported a consistent value of $250-290$nm value for nanoprobe-caging domains within nuclei of different types of cells and organisms (Sec. II B), suggesting a common origin for the domains. As noticed by Valet and Rosa [81], this value

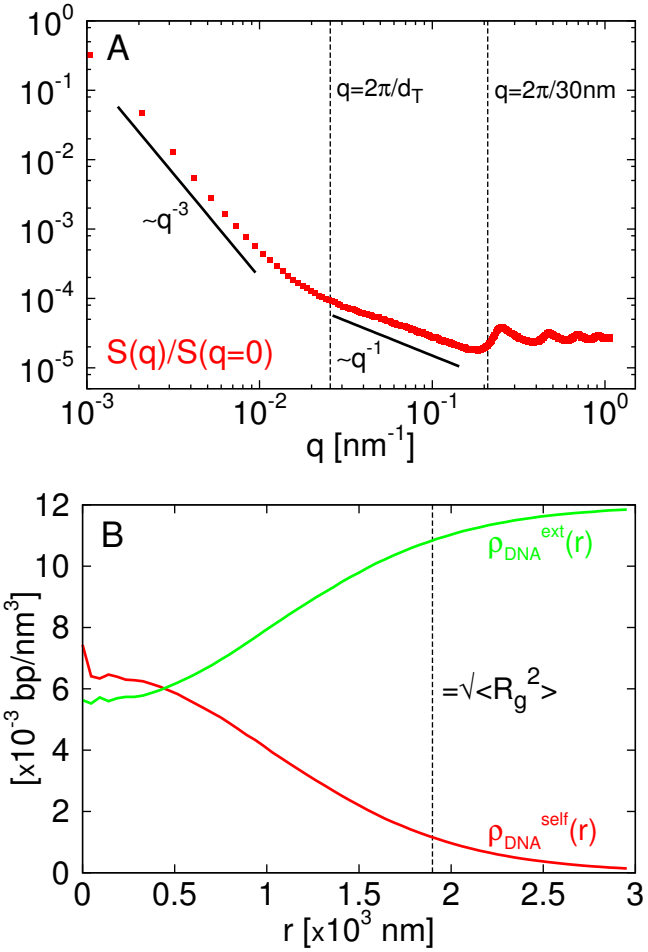

FIG. 9: Predicted spatial structure of model mammalian chromosomes [72, 73]. (A) Structure factor $S(\vec{q})$ *vs.* the norm of the wave vector $q \equiv |\vec{q}|$. The two regimes q^{-1} (rod-like) and q^{-3} (compact-like) are for spatial scales, respectively, below and above the tube diameter, $d_T \approx 245$nm, of the chromatin fiber. The wavy behavior at large q is an artefact due to the discrete bead-spring nature of the model. (B) Average DNA density at spatial distance r from the chromosome centre of mass: $\rho^{\rm self}_{\rm DNA}(r)$, self-density contribution from the given chromosome; $\rho^{\rm ext}_{\rm DNA}(r)$, external contribution from the surrounding chromosomes. The sum of the two equals the average DNA density $= 0.012$bp/nm^3 (Table III). For reference, the dashed line corresponds to the predicted average size of a single chromosome territory.

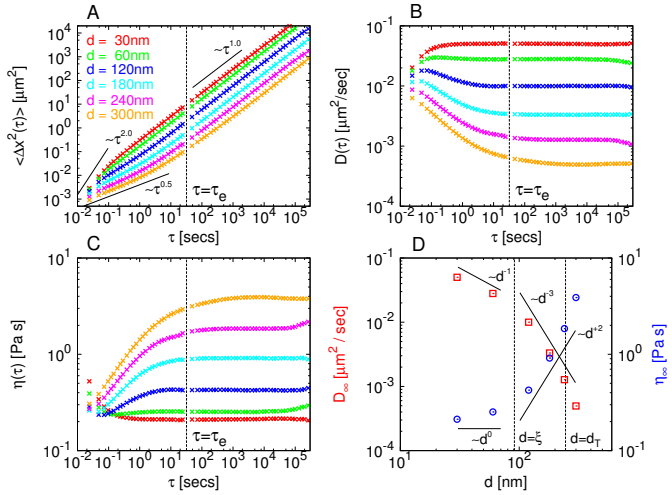

FIG. 10: Viscoelasticity of model interphase chromosomes analysed by microrheology. (A) Time mean-square displacement, $\Delta x^2(\tau)$, of nanoprobes with varying diameter d. Vertical dashed lines mark the position of chromatin entanglement time $\tau_e \approx 32$ seconds [72]. (B) Time-dependent diffusion coefficient, $D(\tau) \equiv \langle \Delta x^2(\tau) \rangle / 6\tau$. (C) Time-dependent viscosities, $\eta(\tau) \equiv \frac{\kappa_B T}{3\pi d\, D(\tau)}$. (D) Asymptotic diffusion coefficient ($\square$), $D_\infty \equiv D(\tau \to \infty)$, and particle viscosity ($\circ$), $\eta_\infty \equiv \eta(\tau \to \infty)$, as functions of nanoprobe diameter, d. Solid lines are for theoretical predictions in the non-entangled regime (Box 2). Polymer-mediated effects start at nanoprobe diameter $d \approx \xi \approx 90$nm (Box 2). The largest nanoprobe diameter is of the order of the tube diameter, $d_T \approx 245$nm, of the chromatin solution. Reproduced with permission from [81].

is also surprisingly close to the nominal tube diameter, $d_T \approx 245$nm, predicted by the "topological" polymer model describing chromosome territories (Sec. III A).

Topological constraints by polymer fibers are likely to induce confinement of dispersed nanoprobes of diameter d if $d \gtrsim d_T$ [82–84]. Motivated by this phenomenon, Valet and Rosa [81] employed large-scale numerical simulations to study the effect of polymer entanglement on the diffusion of nanoprobes of diameter d, and therefore obtain quantitative information for the viscoelastic properties of the nucleoplasm approximated by a semi-dilute solution of chromatin fibers. Different nanoprobes were considered, with d ranging from 30nm (the fiber diameter) to 300nm (slightly above d_T).

Fig. 10 reports the main results, in terms of: (A) nanoprobe time mean-square displacement, $\langle \Delta x^2(\tau) \rangle$; (B) time-dependent diffusion coefficient, $D(\tau) \equiv \frac{\langle \Delta x^2(\tau) \rangle}{6\tau}$; (C) time-dependent viscosity $\eta(\tau) \equiv \frac{\kappa_B T}{3\pi d D(\tau)}$; (D) asymptotic diffusion coefficient ($D_\infty \equiv D(\tau \to \infty)$) and viscosity ($\eta_\infty \equiv \eta(\tau \to \infty)$) *vs.* nanoprobe diameter. The data demonstrate that for d smaller than the polymer correlation length (Box 2) $\xi \approx 90$nm and neglecting the short-time ballistic regime ($\langle \Delta x^2(\tau) \rangle \sim \tau^2$), nanoprobe motion is not or only weakly coupled to chromosome dynamics, implying $\langle \Delta x^2(\tau) \rangle \equiv 6 D_\infty \tau$ with "standard" behaviors $D_\infty \sim d^{-1}$ and $\eta_\infty \sim d^0$. Viceversa, for $d > \xi$ coupling to chromosome dynamics induces nanoprobe subdiffusion ($\langle \Delta x^2(\tau) \rangle \sim \tau^{1/2}$) at small τ and consequent "anomalous" behaviors $D_\infty \sim d^{-3}$ and $\eta_\infty \sim d^2$, in agreement with theoretical predictions (see discussion in Box 2).

Fig. 11 completes the previous analysis by showing (A,B) the distribution functions for D_∞ and (C-E) the distribution functions for particle displacements $\Delta x(\tau) \equiv |x(\tau' + \tau) - x(\tau')|$ at different lag-times τ (see caption for details). In general, D_∞ and $\Delta x(\tau)$ appear Gaussian-

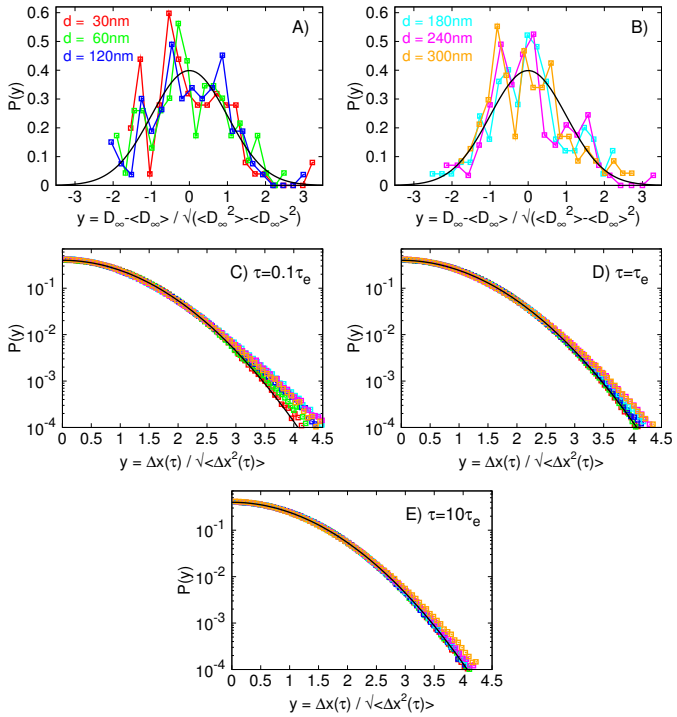

FIG. 11: (A,B) Distribution functions for the asymptotic diffusion coefficients, D_∞. The shape of the distributions compares well to the Gaussian function (black line). (C,D,E) Distribution functions for one-dimensional nanoprobe displacements, $\Delta x(\tau) \equiv |x(t+\tau) - x(t)|$, at different lag-times τ (see corresponding captions). The x-axis have been rescaled according to the corresponding standard deviations $\sqrt{\langle \Delta x^2(\tau) \rangle}$ and the curves compared to the normal form of the Gaussian function describing ordinary diffusion [85]. At $\tau \ll \tau_e$, $P(\Delta x(\tau))$ shifts from Gaussian to non-Gaussian behavior at increasing nanoprobe diameters. Universal Gaussian behavior is recovered at all d's at $\tau \gg \tau_e$. Color code is as in Fig. 10.

distributed (black lines). With one notable exception: for $\tau \ll \tau_e$ and large nanoprobes, $P(\Delta x(\tau))$ appears significantly different from the Gaussian function. This follows from the presence of surrounding polymers exerting constraints and inducing spatial correlations [81] on nanoprobe displacement.

Finally, by using the fundamental relation of microrheology connecting the complex shear modulus to nanoprobe mean-square displacement (Eq. 1 in Box 1), theoretical predictions for the storage and loss moduli at frequency ω can be extracted and then compared to available experimental results, see Table IV. In spite of its simplicity, the polymer model is in reasonable agreement with experiments. The main difference is that experiments predict nuclei with $\hat{G}' > \hat{G}''$ (*i.e.* more solid- than liquid-like, see Box 1), while the polymer model predicts the opposite. Since nanoprobes with diameters larger than d_T should experience a more solid-like behavior (Box 2), this difference can be ascribed to the size of the simulated nanoprobes which is just about d_T. It would be interesting to test then if larger nanoprobes would go more towards the observed experimental behavior.

At the same time, other factors which have not been taken into account because of the initial intention to keep the polymer model as simple as possible could contribute as well to explain deviations from experiments. In the next section, we will comment briefly about these issues and highlight possible directions for future work.

IV. CONCLUSIONS AND FUTURE DIRECTIONS

In this review, we have summarized the results of our efforts to understand chromosome folding and nuclear structure in terms of generic polymer physics. In particular, we have discussed the physical origin of:

1. Chromosome territories. In our framework, the territorial organization of the nucleus (Sec. II A) is explained in terms of the slow Brownian relaxation of non-overlapping long polymer chains subjected to topological constraints (Sec. III A). As a consequence, average chromosome conformations in eukaryotes resemble ring polymers (Fig. 8) with crumpled yet intermingling structure (Fig. 9).

2. Microrheology of the nucleus. The viscoelastic properties of the nucleus (Sec. II B) have been compared to the dynamic behavior of nanoprobes immersed in the ring polymers solution (Sec. III B). The model is in good quantitative agreement with theoretical expectations (Fig. 10) and in qualitative agreement with available experiments for nuclear microrheology (Table IV).

Obviously, due to the complexity of the genome and the simplicity of the model, it is no surprise that there is still much work ahead which remains to be done in order to arrive to a satisfactory picture of genome organization in terms of polymer physics. In this spirit, in the following we discuss a few promising directions which should be undertake to make the model more coherent with experimental data.

First, an evident inconsistency between the outcome of microrheology experiments and the results of our polymer model is in the latter showing no sign of a plateau in the time MSD or the storage modulus $G'(\omega)$ (compare Fig. 3(A,B) of Ref. [40] to Fig. 10(A)), in spite of the very similar sizes of nanoprobes used. It should be possible to "level" this discrepancy though, by introducing a fixed amount of long-lived or permanent *cross-links* between chromatin fibers. Cross-links are known to quench polymer dynamics without altering significantly the average polymer $3d$ structure [86] and may affect nanoprobe diffusive behavior when its size becomes larger than the polymer tube diameter [87]. On the biological side, there exist a conspicuous number of experimental observations [4, 32, 88] proving the existence of

Microrheology of the nucleus: theoretical predictions from Ref. [81]

			0.1 Hz		1 Hz		10 Hz	
d [nm]	D_∞ [$\times 10^{-3}\mu\mathrm{m}^2\cdot\mathrm{s}^{-1}$]	η_∞ [Pa · s]	$\hat{G}'$ [Pa]	$\hat{G}''$ [Pa]	$\hat{G}'$ [Pa]	$\hat{G}''$ [Pa]	$\hat{G}'$ [Pa]	$\hat{G}''$ [Pa]
30	50.0	0.21	–	0.0214	–	0.2045	–	2.0651
60	28.0	0.25	0.0004	0.0238	0.0079	0.2532	–	2.2061
120	10.0	0.42	–	0.0423	0.0712	0.3948	0.7009	2.3778
180	3.3	0.92	0.0086	0.0882	0.2260	0.6865	1.6126	2.8336
240	1.3	1.81	0.0349	0.1469	0.4959	1.0163	2.6690	3.5608
300	0.5	3.86	0.0747	0.2972	0.8674	1.4476	3.7901	4.5105

Microrheology of the nucleus: experiments

d [nm]	Organism	Frequency [Hz]	$\hat{G}'$ [Pa]	$\hat{G}''$ [Pa]
100	Swiss 3T3 fibroblasts (mouse) [40]	$1-10$	≈ 10	$\approx 3-10$
1000	HeLa cells (human) [54]	1	≈ 0.1	≈ 0.05

TABLE IV: Microrheology of the nucleus: theoretical modeling (top) *vs.* experiments (bottom). Asymptotic diffusion coefficients (D_∞), viscosities (η_∞) and selected values for storage ($\hat{G}'(\omega)$) and loss ($\hat{G}''(\omega)$) moduli. The symbol "–" means no data are available.

functionally-relevant protein bridges between sequence-distant chromatin loci which, indeed, may act as effective cross-links. In this respect then, numerical investigations of nanoprobe dynamics could help estimating the specific amount of cross-links present in the genome and elucidating their role in chromatin organization.

Second, a few recent studies [48, 54] have demonstrated that chromosome activity and chromosome dynamics consist of the subtle interplay between *passive* thermal diffusion and *active*, ATP-dependent motion triggered by chromatin remodeling and transcription complexes. Stimulated by active processes, chromatin dynamics influences also the motion of dispersed nanoprobes [54]. Taken together, these results suggest that the standard picture adopted so far where chromatin is modeled as a passive polymer is an oversimplification. In recent years, non-equilibrium physics of active systems [89] and active polymers [90] has received considerable attention for its being at the interface between statistical, soft matter and biological physics. To our knowledge, the first attempt to include activity in a numerical polymer model for eukaryotic chromosomes was due to Ganai *et al.* [91] who argued that non-random chromosome segregation is the result of differences in *non-equilibrium* activity across chromosomes originating in the inhomogeneous distribution of ATP-dependent chromatin remodeling and transcription machinery on each chromosome. In their model, each monomer is characterized by a given transcription level whose fluctuations are suitably taken into account by a local "effective" temperature: "hot" (respectively, "cold") monomers are associated to active and gene-rich (resp., inactive and gene-poor) monomers. Through a similar approach and rigorous theoretical considerations, Smrek and Kremer [92] showed that entangled polymer solutions where single chains have different temperatures undergo *non-equilibrium* phase separation similarly to classical *equilibrium* phase separation observed in polymer mixtures [74]. As in the afore mentioned case of transcription or in the recently proposed looping extrusion mechanism [93], active processes play a fundamental role in chromosome organization. It would be interesting, then, to explore to which extent the viscoelastic properties of chromatin fibers are changed by the presence of non-equilibrium mechanisms.

To conclude, we hope having convinced the reader that polymer physics represents a fundamental tool to describe and predict chromosome structure during the different stages of the cell cycle. In general, the conspicuous amount of experimental data currently being published is causing the field to boom and many different polymer models (see, for instance, Ref. [11]) are available at present. The specificity of the point of view adopted here (and in our work [72, 73, 78, 81] on which this review is based) consists in the assumption that topological constraints are an *essential* feature to be retained in all minimal polymer models. In particular, a quantitative understanding of this "null model" with the inclusion of proper mapping [72] to real time and length scales is a prerequisite for attempts [94–99] to reconstruct or predict the three-dimensional chromosome structure and the dynamics of entire cell nuclei, and provide then a reliable description of the large-scale structure and dynamics of nuclear compartmentalization.

[1] J. Dekker, A. S. Belmont, M. Guttman, V. O. Leshyk, J. T. Lis, S. Lomvardas, L. A. Mirny, C. C. O'Shea, P. J. Park, B. Ren, et al., Nature **549**, 219 (2017).

[2] http://www.4dnucleome.eu/.

[3] T. Cremer and C. Cremer, Nature Rev. Genet. **2**, 292 (2001).

[4] E. Lieberman-Aiden et al., Science **326**, 289 (2009).

[5] S. M. Gasser, Science **296**, 1412 (2002).

Box 1. Principles of particle-tracking microrheology.

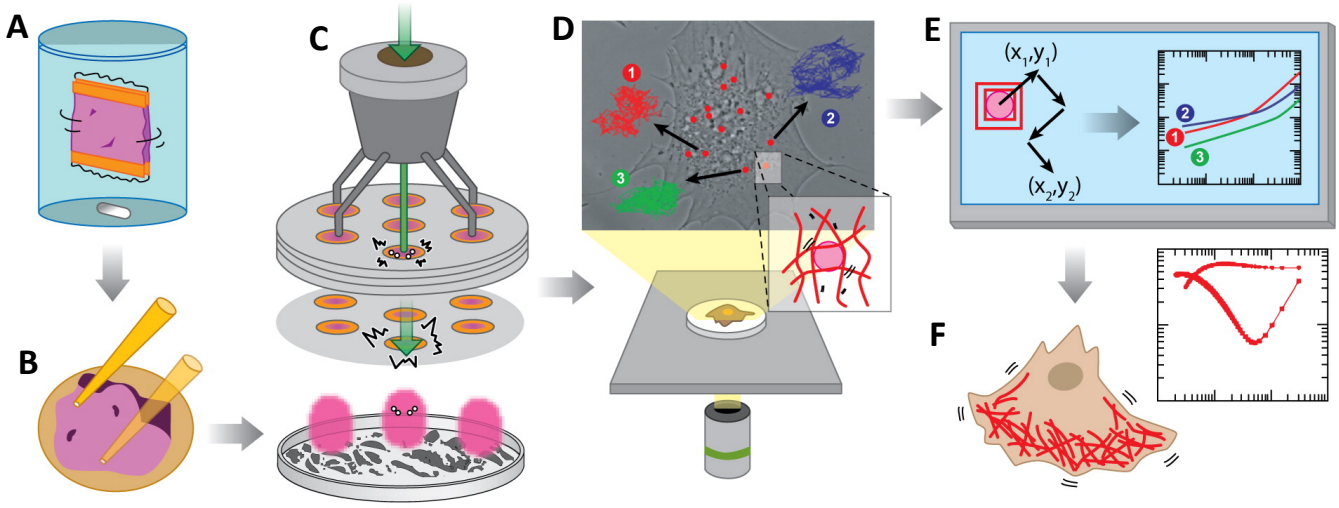

Sequential steps in microrheology: (A) After the initial preparation of the sub-micron fluorescent probes, (B) the beads are spread on a grid and (C) ballistically injected inside the cytoplasm where they rapidly disperse. (D) The cells are then placed under a fluorescence microscope and the random motion of the probes is monitored with high spatial and temporal resolutions. Examples of three trajectories are shown in red (1), blue (2), green (3). (E) The recorded time-dependent coordinates, $\vec{x}(t)$, of the probes are transformed into time-lag mean-square displacements (MSDs). (F) Finally, the MSDs of the probes are used to derive the local values of the frequency-dependent storage ($\hat{G}'(\omega)$) and loss ($\hat{G}''(\omega)$) moduli of the cytoplasm and/or the nucleoplasm. Reproduced with permission from [7].

Microrheology exploits the erratic (Brownian) motion of fluorescent nanoprobes (figure) carefully injected inside the cytoplasm or the nucleus as a proxy for the viscoelastic properties of the embedding medium [7, 40–43]. Compared to standard (bulk) rheology, microrheology grants systematic screening over wide ranges of length and time scales for the feasibility of designing trackable nanoprobes of linear sizes ranging from only a few nanometers [100] to hundreds of nanometers [40] and microns [54]. Microrheology is nowadays especially suitable for studies of biological materials [43] since, being minimally invasive, it allows to perform experiments *in vivo* and with very small samples [41].

Experimental data for microrheology can be obtained by various means, such as dynamic light scattering (DLS) [101]. More commonly, the motion of the probe in the form of its spatial coordinates (figure) can be recorded through direct imaging and transformed into the time mean-square displacement, $\langle \Delta x^2(\tau) \rangle \equiv \frac{1}{\mathcal{T}-\tau} \int_0^{\mathcal{T}-\tau} (\vec{x}(t+\tau) - \vec{x}(t))^2 dt$, where $\mathcal{T}$ is the measurement time and τ the lag-time [44]. Then, the viscoelasticity of the embedding medium and nanoprobe motion are connected by the following mathematical relation [102]:

$$\hat{G}(\omega) = -i \frac{2\kappa_B T}{\pi d\, \omega\, \langle \Delta \hat{x}^2(\omega) \rangle} \,. \tag{1}$$

Here: $i = \sqrt{-1}$ is the imaginary unit; κ_B is the Boltzmann constant; T is the absolute temperature; d is the nanoprobe diameter; $\langle \Delta \hat{x}^2(\omega) \rangle$ is the Laplace-Fourier (LF) transform of $\langle \Delta x^2(\tau) \rangle$ (ω is the frequency). $\hat{G}(\omega) \equiv \hat{G}'(\omega) + i\hat{G}''(\omega)$ is the complex *shear modulus* of the medium: its real ($\hat{G}'(\omega)$) and imaginary ($\hat{G}''(\omega)$) parts correspond to the storage (elastic) and loss (viscous) moduli [74], respectively.

To illustrate the method, we consider the general situation where nanoprobe diffusion is power-law-like [45]: $\langle \Delta x^2(\tau) \rangle = 6 D_\alpha \tau^\alpha$, where D_α is the (generalized) diffusion coefficient ($0 \le \alpha \le 1$) and τ is the lag-time. With the corresponding LF-transform given by $\langle \Delta \hat{x}^2(\omega) \rangle = 6 D_\alpha\, \Gamma(\alpha+1)\, (i\omega)^{-(\alpha+1)}$, $\hat{G}'(\omega)$ and $\hat{G}''(\omega)$ are expressed by the simple formulas:

$$\hat{G}'(\omega) = \frac{\kappa_B T}{3\pi d} \frac{\cos(\pi\alpha/2)}{D_\alpha\, \Gamma(\alpha+1)} \omega^\alpha \,, \quad \hat{G}''(\omega) = \frac{\kappa_B T}{3\pi d} \frac{\sin(\pi\alpha/2)}{D_\alpha\, \Gamma(\alpha+1)} \omega^\alpha \,. \tag{2}$$

The two "special" limits of $\alpha = 0$ and $\alpha = 1$ correspond, respectively, to the well-known cases of $\hat{G}(\omega) = \hat{G}'(\omega) = const = \frac{\kappa_B T}{3\pi d\, D_0}$ and $\hat{G}(\omega) = i\hat{G}''(\omega) = i \frac{\kappa_B T}{3\pi d\, D_1} \omega \equiv i\eta\omega$. In the former case the medium responds as an elastic (Hookean) solid, while in the latter its behavior is as of a classical fluid with "bulk" viscosity $= \eta$. In the intermediate case of $0 < \alpha < 1$ both, $\hat{G}'(\omega)$ and $\hat{G}''(\omega)$, are non-zero and the medium displays intermediate (solid/liquid) properties.

Box 2. Structure and microrheology of entangled ring polymers in solution.

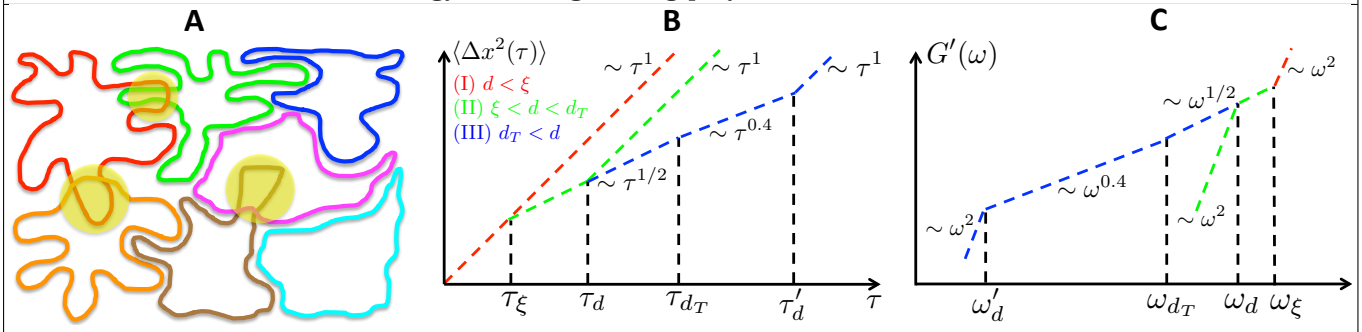

(A) Schematic illustration of ring polymers in dense solution. Shaded areas highlight threadings between close-by chains. (B) Time mean-square displacement $\langle \Delta x^2(\tau) \rangle$ of nanoprobes in solutions of ring polymers. (C) Corresponding predictions (obtained by using Eqs. 1 and 2) for the storage modulus $G'(\omega)$ as function of frequency ω. Each crossover frequency is the inverse of the corresponding crossover time in panel (B) multiplied by "2π". An analogous plot for the loss modulus $G''(\omega)$ can be constructed. Plots are in log-log scales.

Structure – Ring polymers in entangled solutions have to respect global topological invariance requiring that all chains remain permanently *unlinked* at the expense of entropic loss [103]. Consequently, topological constraints between close-by rings induce chain conformations to fold into compact (*i.e.*, "territorial" [104]) structures which are reminiscent of the "crumpled" (or "fractal" [4]) globule [105–108]. Recent numerical work [73, 109, 110] has confirmed this conjecture and, thus, demonstrated that the typical end-to-end mean-square spatial distance between chain monomers with contour separation L is given by:

$$\langle R^2(L) \rangle \approx \begin{cases} L^2\,, & L \lesssim \ell_K \\ \ell_K L\,, & \ell_K \lesssim L \lesssim L_e \\ \ell_K L_e \left(\frac{L}{L_e}\right)^{2/3}\,, & L \gtrsim L_e \end{cases} . \tag{3}$$

ℓ_K is the Kuhn length of the polymer describing chain stiffness [74]. L_e, which depends on ℓ_K and solution density ρ [77, 111], is the so-called *entanglement* length marking the onset of entanglement effects. The corresponding end-to-end spatial distance between entanglement strands $d_T \approx (\ell_K L_e)^{1/2}$ (the "entanglement distance") is also called the "tube diameter" by analogy to systems of linear chains [75]. Amongst their noticeable features and in spite of compactess, rings do not expel close-by rings: on average in fact their surface remains "rough" and shares many contacts with neighbors [108, 110, 112, 113]. Indeed, rings interpenetrate as "threading" conformations [114, 115] (figure, panel (A)) akin to interacting "branched structures" [73] with long-range (loose) loops [116, 117].

Microrheology – Depending on nanoprobe diameter three regimes (figure, panel (B)) can be distinguished [82–84]:

I) Small nanoprobes, $d \lesssim \xi$, where ξ (the "correlation length") is the average distance from a monomer on one chain to the nearest monomer on another chain [74]. Nanoprobes interact only with the solvent, and their motion remains diffusive:

$$\langle \Delta x^2(\tau) \rangle \sim D_s\, \tau \sim \frac{\kappa_B T}{\eta_s\, d}\, \tau\,. \tag{4}$$

D_s is the diffusion coefficient and η_s is the viscosity of the solvent.

II) Intermediate nanoprobes, $\xi \lesssim d \lesssim d_T$. Nanoprobe motion is now affected by the polymers, showing three regimes:

$$\langle \Delta x^2(\tau) \rangle \sim \begin{cases} D_s\, \tau, & \tau < \tau_\xi \sim \frac{\eta_s \xi^3}{\kappa_B T} \quad \text{(II.a)} \\ D_s \tau_\xi \left(\frac{\tau}{\tau_\xi}\right)^{1/2}, & \tau_\xi < \tau < \tau_d \sim \tau_\xi \left(\frac{d}{\xi}\right)^4 \quad \text{(II.b)} \\ D_s \left(\frac{\xi}{d}\right)^2 \tau, & \tau > \tau_d \quad \text{(II.c)} \end{cases} \tag{5}$$

In (II.a), nanoprobe motion is driven only by random collisions with the solvent, as in (I). This regime stops at τ_ξ, the relaxation time of a polymer strand of spatial size ξ. Then (II.b), the nanoprobe experiences a time-dependent viscosity $\eta(\tau) \sim \eta_s\, n_{str}(\tau) \equiv \eta_s\, (\tau/\tau_\xi)^{1/2}$, where $n_{str}(\tau)$ is the number of strands which have relaxed at time τ. This regime stops at time τ_d, the relaxation time of a larger polymer strand of spatial size $= d = \xi \sqrt{n_{str}(\tau_d)}$. Above τ_d (II.c), nanoprobe motion becomes diffusive again with effective viscosity $\sim \eta_s\, n_{str}(\tau_d)$, which is $\sim (d/\xi)^2$ times *larger* than the value in pure solvent.

III) Large nanoprobes, $d \gtrsim d_T$. Regime (II.a) still holds, while regime (II.b) stops at $\tau_{d=d_T} = \tau_\xi\, (d_T/\xi)^4$. Above τ_{d_T}, entanglements affect nanoprobe motion. By scaling arguments [74], the time-dependent friction $\eta = \eta(\tau) \approx \tau G(\tau)$ where: $G(\tau) \sim \frac{\kappa_B T}{\nu^{2/3} L(\tau)}$ is the stress relaxation modulus, ν is the monomer volume and $L(\tau) \sim L_e\, (\tau/\tau_e)^{1/\gamma}$ ($\gamma = 2.33 - 2.57$ [116, 118, 119]) is the contour length of the polymer strand with relaxation time τ. Therefore,

$$\langle \Delta x^2(\tau) \rangle \sim \frac{\kappa_B T}{\eta(L(\tau))d}\, \tau \sim \frac{\nu^{2/3} L_e}{d} \left(\frac{\tau}{\tau_e}\right)^{1/\gamma}\,, \tag{6}$$

and nanoprobe diffusion is anomalous with exponent $1/\gamma = 0.39 - 0.43$. This regime breaks down at $\tau'_d \sim \tau_e \left(d^2/(\ell_K L_e)\right)^{3\gamma/2} = \tau_e \left(d^2/(\ell_K L_e)\right)^{3.50-3.86}$, the relaxation time of a ring strand of spatial extension $\approx d$ in the compact regime (Eq. 3 for $L \gtrsim L_e$). For $\tau > \tau'_d$, nanoprobe diffusion is normal with $\langle \Delta x^2(\tau) \rangle \sim \frac{\kappa_B T}{\eta(L(\tau'_d))d}\, \tau$.

By applying Eqs. 1 and 2 (Box 1), the shapes of the storage and loss moduli can be then recovered (figure, panel (C)).

[6] K. Bystricky, FEBS Lett. **589**, 3014 (2015).
[7] D. Wirtz, Annu. Rev. Biophys. **38**, 301 (2009).
[8] M. Forcato, C. Nicoletti, K. Pal, C. M. Livi, F. Ferrari, and S. Bicciato, Nat. Methods **14**, 679 (2017).
[9] M. W. Libbrecht and W. S. Noble, Nat. Rev. Genet. **16**, 321 (2015).
[10] J. Dekker, M. A. Marti-Renom, and L. A. Mirny, Nat. Rev. Genet. **14**, 390 (2013).
[11] A. Rosa and C. Zimmer, Int. Rev. Cell Mol. Biol. **307**, 275 (2014).
[12] A. M. Chiariello, C. Annunziatella, S. Bianco, A. Esposito, and M. Nicodemi, Sci. Rep. **6**, 29775 (2016).
[13] D. Jost, C. Vaillant, and P. Meister, Curr. Opin. Cell Biol. **44**, 20 (2017).
[14] C. Lanctôt, T. Cheutin, M. Cremer, G. Cavalli, and T. Cremer, Nat. Rev. Genet. **8**, 104 (2007).
[15] B. Alberts et al., *Molecular Biology of the Cell* (Garland Science, New York, 2007), 5^{th} ed.
[16] T. Cremer and M. Cremer, Cold Spring Harbor Perspectives in Biology **2**, 1 (2010).
[17] J. H. Gibcus and J. Dekker, Molecular Cell **49**, 773 (2013).
[18] I. Solovei, M. Kreysing, C. Lanctôt, S. Kösem, L. Peichl, T. Cremer, J. Guck, and B. Joffe, Cell **137**, 356 (2009).
[19] M. Columbaro, C. Capanni, E. Mattioli, G. Novelli, V. Parnaik, S. Squarzoni, N. Maraldi, and G. Lattanzi, Cell. Mol. Life Sci. **62**, 2669 (2005).
[20] R. P. McCord, A. Nazario-Toole, H. Zhang, P. S. Chines, Y. Zhan, M. R. Erdos, F. S. Collins, J. Dekker, and K. Cao, Genome Res. **23**, 260 (2013).
[21] T. Chandra, P. A. Ewels, S. Schoenfelder, M. Furlan-Magaril, S. W. Wingett, K. Kirschner, J.-Y. Thuret, S. Andrews, P. Fraser, and W. Reik, Cell Reports **10**, 471 (2015).
[22] A. J. Fritz, B. Stojkovic, H. Ding, J. Xu, S. Bhattacharya, D. Gaile, and R. Berezney, Hum. Mol. Genet. **23**, 5133 (2014).
[23] H. K. Norton and J. E. Phillips-Cremins, J. Cell Biol. **216**, 3441 (2017).
[24] J. C. Hansen, Annu. Rev. Biophys. Biomol. Struct. **31**, 361 (2002).
[25] K. Luger, A. W. Mader, R. K. Richmond, D. F. Sargent, and T. J. Richmond, Nature **389**, 251 (1997).
[26] K. Luger and J. C. Hansen, Curr. Opin. Struct. Biol. **15**, 188 (2005).
[27] K. Maeshima, R. Imai, T. Hikima, and Y. Joti, Methods **70**, 154 (2014).
[28] K. Maeshima, S. Ide, K. Hibino, and M. Sasai, Curr. Opin. Genet. Dev. **37**, 36 (2016).
[29] H. D. Ou, S. Phan, T. J. Deerinck, A. Thor, M. H. Ellisman, and C. C. O'Shea, Science **357** (2017).
[30] V. Récamier, I. Izeddin, L. Bosanac, M. Dahan, F. Proux, and X. Darzacq, Nucleus **5**, 75 (2014).
[31] M. R. Speicher and N. P. Carter, Nat. Rev. Genet. **6**, 782 (2005).
[32] J. R. Dixon, S. Selvaraj, F. Yue, A. Kim, Y. Li, Y. Shen, M. Hu, J. S. Liu, and B. Ren, Nature **485**, 376 (2012).
[33] W. F. Marshall, Curr. Biol. **12**, R185 (2002).
[34] M. R. Branco and A. Pombo, Plos Biol. **4**, e138 (2006).
[35] A. Bolzer, G. Kreth, I. Solovei, D. Koehler, K. Saracoglu, C. Fauth, S. Muller, R. Eils, C. Cremer, M. Speicher, et al., Plos Biol. **3**, 826 (2005).
[36] J. R. Dixon, I. Jung, S. Selvaraj, Y. Shen, J. E. Antosiewicz-Bourget, A. Y. Lee, Z. Ye, A. Kim, N. Rajagopal, W. Xie, et al., Nature **518**, 331 (2015).
[37] N. Lonfat, T. Montavon, F. Darbellay, S. Gitto, and D. Duboule, Science **346**, 1004 (2014).
[38] A. Bancaud, S. Huet, N. Daigle, J. Mozziconacci, J. Beaudouin, and J. Ellenberg, Embo J. **28**, 3785 (2009).
[39] S. Hihara, C.-G. Pack, K. Kaizu, T. Tani, T. Hanafusa, T. Nozaki, S. Takemoto, T. Yoshimi, H. Yokota, N. Imamoto, et al., Cell Reports **2**, 1645 (2012).
[40] Y. Tseng, J. S. H. Lee, T. P. Kole, I. Jiang, and D. Wirtz, J. Cell Sci. **117**, 2159 (2004).
[41] P. Cicuta and A. Donald, Soft Matter **3**, 1449 (2007).
[42] P.-H. Wu, C. M. Hale, W.-C. Chen, J. S. H. Lee, Y. Tseng, and D. Wirtz, Nat. Protocols **7**, 155 (2012).
[43] T. A. Waigh, Rep. Prog. Phys. **79**, 074601 (2016).
[44] R. Metzler, J.-H. Jeon, A. G. Cherstvy, and E. Barkai, Phys. Chem. Chem. Phys. **16**, 24128 (2014).
[45] M. J. Saxton, Biophys. J. **66**, 394 (1994).
[46] J.-P. Bouchaud and A. Georges, Phys. Rep. **195**, 127 (1990).
[47] I. Bronshtein, I. Kanter, E. Kepten, M. Lindner, S. Berezin, Y. Shav-Tal, and Y. Garini, Nucleus **7**, 27 (2016).
[48] S. C. Weber, A. J. Spakowitz, and J. A. Theriot, Proc. Natl. Acad. Sci. USA **109**, 7338 (2012).
[49] A. Zidovska, D. A. Weitz, and T. J. Mitchison, Proc. Natl. Acad. Sci. USA **110**, 15555 (2013).
[50] D. Marenduzzo, K. Finan, and P. R. Cook, J. Cell Biol. **175**, 681 (2006).
[51] S. Huet, C. Lavelle, H. Ranchon, P. Carrivain, J.-M. Victor, A. Bancaud, R. Hancock, and K. W. Jeon, Int. Rev. Cell Mol. Biol. **307**, 443 (2014).
[52] H. Hajjoul, J. Mathon, H. Ranchon, I. Goiffon, J. Mozziconacci, B. Albert, P. Carrivain, J.-M. Victor, O. Gadal, K. Bystricky, et al., Genome Res. **23**, 1829 (2013).
[53] Y. Tseng, T. P. Kole, S.-H. J. Lee, and D. Wirtz, Curr. Opin. Colloid In. **7**, 210 (2002).
[54] F. M. Hameed, M. Rao, and G. Shivashankar, Plos One **7**, e45843 (2012).
[55] M. Carmo-Fonseca, M. Platani, and J. R. Swedlow, Trends Cell Biol. **12**, 491 (2002).
[56] M. Platani, I. G. Goldberg, D. Bensaddek, and J. R. Swedlow, Nat. Cell Biol. **4**, 502 (2002).
[57] S. M. Görisch, M. Wachsmuth, C. Ittrich, C. P. Bacher, K. Rippe, and P. Lichter, Proc. Natl. Acad. Sci. USA **101**, 13221 (2004).
[58] D. K. Sinha, B. Banerjee, S. Maharana, and G. V. Shivashankar, Biophys. J. **95**, 5432 (2008).
[59] A. D. Conger and J. H. Clinton, Radiation Research **54**, 69 (1973).
[60] http://www.genomesize.com.
[61] G. Maul and L. Deaven, J. Cell Biol. **73**, 748 (1977).
[62] K. P. Baetcke, A. H. Sparrow, C. H. Nauman, and S. S. Schwemmer, Proc. Natl. Acad. Sci. USA **58**, 533 (1967).
[63] H. J. Price, A. H. Sparrow, and A. F. Nauman, Experientia **29**, 1028 (1973).
[64] http://data.kew.org/cvalues.
[65] A. H. Sparrow, A. F. Rogers, and S. S. Schwemmer, Radiation Botany **8**, 149 (1968).
[66] M. Emanuel, N. H. Radja, A. Henriksson, and H. Schiessel, Phys. Biol. **6**, 025008 (2009).
[67] J. Mateos-Langerak et al., Proc. Natl. Acad. Sci. USA **106**, 3812 (2009).
[68] L. A. Mirny, Chromosome Res. **19**, 37 (2011).

[69] J. D. Halverson, J. Smrek, K. Kremer, and A. Y. Grosberg, Rep. Prog. Phys. **77**, 022601 (2014).
[70] C. A. Brackley, J. Johnson, S. Kelly, P. R. Cook, and D. Marenduzzo, Nucleic Acids Res. **44**, 3503 (2016).
[71] D. Jost, A. Rosa, C. Vaillant, and R. Everaers, in *Nuclear Architecture and Dynamics, Volume 2*, edited by C. Lavelle and J.-M. Victor (Academic Press, 2017).
[72] A. Rosa and R. Everaers, Plos Comput. Biol. **4**, e1000153 (2008).
[73] A. Rosa and R. Everaers, Phys. Rev. Lett. **112**, 118302 (2014).
[74] M. Rubinstein and R. H. Colby, *Polymer Physics* (Oxford University Press, New York, 2003).
[75] M. Doi and S. F. Edwards, *The Theory of Polymer Dynamics* (Oxford University Press, New York, 1986).
[76] K. Bystricky, P. Heun, L. Gehlen, J. Langowski, and S. M. Gasser, Proc. Natl. Acad. Sci. USA **101**, 16495 (2004).
[77] T. A. Kavassalis and J. Noolandi, Phys. Rev. Lett. **59**, 2674 (1987).
[78] A. Rosa, N. B. Becker, and R. Everaers, Biophys. J. **98**, 2410 (2010).
[79] A.-M. Florescu, P. Therizols, and A. Rosa, Plos. Comput. Biol. **12**, e1004987 (2016).
[80] A. Louis, P. Bolhuis, J. Hansen, and E. Meijer, Phys. Rev. Lett. **85**, 2522 (2000).
[81] M. Valet and A. Rosa, J. Chem. Phys. **141**, 245101 (2014).
[82] L.-H. Cai, S. Panyukov, and M. Rubinstein, Macromolecules **44**, 7853 (2011).
[83] L.-H. Cai, S. Panyukov, and M. Rubinstein, Macromolecules **48**, 847 (2015).
[84] T. Ge, J. T. Kalathi, J. D. Halverson, G. S. Grest, and M. Rubinstein, Macromolecules **50**, 1749 (2017).
[85] N. G. Van Kampen, *Stochastic Processes in Physics and Chemistry* (Elsevier, Amsterdam, 2007), 3rd ed.
[86] R. T. Deam and S. F. Edwards, Philos. T. Roy. Soc. A **280**, 317 (1976).
[87] J. T. Kalathi, U. Yamamoto, K. S. Schweizer, G. S. Grest, and S. K. Kumar, Phys. Rev. Lett. **112**, 108301 (2014).
[88] P. R. Cook, J. Mol. Biol. **395**, 1 (2010).
[89] G. De Magistris and D. Marenduzzo, Physica A **418**, 65 (2015).
[90] R. G. Winkler, J. Elgeti, and G. Gompper, J. Phys. Soc. Jpn. **86**, 101014 (2017).
[91] N. Ganai, S. Sengupta, and G. I. Menon, Nucleic Acids Res. **42**, 4145 (2014).
[92] J. Smrek and K. Kremer, Phys. Rev. Lett. **118**, 098002 (2017).
[93] A. Goloborodko, J. F. Marko, and L. A. Mirny, Biophys. J. **110**, 2162 (2016).
[94] D. Baù et al., Nat. Struct. Mol. Biol. **18**, 107 (2011).
[95] H. Wong et al., Curr. Biol. **22**, 1881 (2012).
[96] M. Di Stefano, A. Rosa, V. Belcastro, D. di Bernardo, and C. Micheletti, Plos Comput. Biol. **9**, e1003019 (2013).
[97] F. Serra, M. Di Stefano, Y. G. Spill, Y. Cuartero, M. Goodstadt, D. Baù, and M. A. Marti-Renom, FEBS Lett. **589**, 2987 (2015).
[98] M. Di Stefano, J. Paulsen, T. G. Lien, E. Hovig, and C. Micheletti, Sci. Rep.-UK **6**, 35985 (2016).
[99] G. Tiana and L. Giorgetti, Curr. Opin. Struc. Biol. **49**, 11 (2018).
[100] G. Guigas, C. Kalla, and M. Weiss, Biophys. J. **93**, 316 (2007).
[101] A. M. Puertas and T. Voigtmann, J. Phys.-Condens. Matter **26**, 243101 (2014).
[102] T. G. Mason and D. A. Weitz, Phys. Rev. Lett. **74**, 1250 (1995).
[103] M. E. Cates and J. M. Deutsch, J. Phys. (Paris) **47**, 2121 (1986).
[104] T. Vettorel, A. Y. Grosberg, and K. Kremer, Phys. Today **62**, 72 (2009).
[105] A. R. Khokhlov and S. K. Nechaev, Phys. Lett. **112A**, 156 (1985).
[106] A. Y. Grosberg, S. K. Nechaev, and E. I. Shakhnovich, J. Phys. France **49**, 2095 (1988).
[107] A. Grosberg, Y. Rabin, S. Havlin, and A. Neer, Europhys. Lett. **23**, 373 (1993).
[108] A. Y. Grosberg, Soft Matter **10**, 560 (2014).
[109] J. Suzuki, A. Takano, T. Deguchi, and Y. Matsushita, J. Chem. Phys. **131**, 144902 (2009).
[110] J. D. Halverson, W. B. Lee, G. S. Grest, A. Y. Grosberg, and K. Kremer, J. Chem. Phys. **134**, 204904 (2011).
[111] N. Uchida, G. S. Grest, and R. Everaers, J. Chem. Phys. **128**, 044902 (2008).
[112] J. D. Halverson, K. Kremer, and A. Y. Grosberg, J. Phys. A: Math. Theor. **46**, 065002 (2013).
[113] J. Smrek and A. Y. Grosberg, ACS Macro Lett. **5**, 750 (2016).
[114] W.-C. Lo and M. S. Turner, EPL **102**, 58005 (2013).
[115] D. Michieletto, D. Marenduzzo, E. Orlandini, G. P. Alexander, and M. S. Turner, ACS Macro Lett. **3**, 255 (2014).
[116] T. Ge, S. Panyukov, and M. Rubinstein, Macromolecules **49**, 708 (2016).
[117] D. Michieletto, Soft Matter **12**, 9485 (2016).
[118] S. P. Obukhov, M. Rubinstein, and T. Duke, Phys. Rev. Lett. **73**, 1263 (1994).
[119] J. Smrek and A. Y. Grosberg, J. Phys.-Condens. Matter **27**, 064117 (2015).